

A Brisk Estimator for the Angular Multipoles (BEAM) of the redshift space bispectrum.

Sukhdeep Singh Gill* and Somnath Bharadwaj†

Department of Physics, Indian Institute of Technology Kharagpur, Kharagpur 721302, India.

The anisotropy of the redshift space bispectrum depends upon the orientation of the triangles formed by three \mathbf{k} modes with respect to the line of sight. For a triangle of fixed size (k_1) and shape (μ, t), this orientation dependence can be quantified in terms of angular multipoles $B_\ell^m(k_1, \mu, t)$ which contain a wealth of cosmological information. We propose a fast and efficient FFT-based estimator that computes bispectrum multipole moments B_ℓ^m of a 3D cosmological field for all possible ℓ and m (including $m \neq 0$). The time required by the estimator to compute all multipoles from a gridded data cube of volume N_g^3 scales as $\sim N_g^3 \log(N_g)$ in contrast to the direct computation technique which requires time $\sim N_g^6$. Here, we demonstrate the formalism and validate the estimator using a simulated non-Gaussian field for which the analytical expressions for all bispectrum multipoles are known. The estimated results are found to be in good agreement with the analytical predictions for all 16 non-zero multipoles (up to $\ell = 6, m = 6$). We expect the $m \neq 0$ bispectrum multipoles to significantly enhance the information available from galaxy redshift surveys, and future redshifted 21-cm observations.

I. INTRODUCTION

The spatial distribution of galaxies has emerged as one of the primary probes of large-scale structure (LSS) of the Universe. The simplest model of inflation predicts the primordial density fluctuations that seed the LSS to be a Gaussian random field. Nevertheless, the subsequent non-linear growth and non-linear biasing induce non-Gaussianity in the galaxy distribution. Further, many inflationary paradigms speculate non-Gaussian primordial fluctuations. In any scenario, it is essential to exploit the statistics that capture the non-Gaussian nature of galaxy distribution and utilize the maximum potential of data from surveys such as SDSS¹ [1], DESI² [2], LSST³ [3], and EUCLID⁴ [4]. Bispectrum is the lowest-order statistic sensitive to non-Gaussianity in the underlying distribution. It is a function of closed triangles formed by three \mathbf{k} vectors and contains the information on mode coupling. The inclusion of bispectrum significantly supplements our comprehension of the standard model of cosmology, enabling robust constraints on the primordial non-Gaussianity [5–15], modeling the inflation [16–18], lifting the degeneracy between Ω_m and b_1 [19], constraining cosmological parameters [20–22], and galaxy bias parameters [23].

The observed galaxy bispectrum is anisotropic along the line of sight direction caused by the peculiar motion of galaxies. This anisotropy of the redshift space bispectrum can be studied by decomposing it into spherical harmonic $Y_\ell^m(\hat{p})$ basis [24–26]. The expansion coefficients in $Y_\ell^m(\hat{p})$ basis, bispectrum multipole moments B_ℓ^m , can be measured from the survey data. While the majority of

work has focused on monopole moment B_0^0 only [21], the measurements of few higher order multipoles have also been utilized to constrain cosmologies [20, 22, 27–29]. To the best of our knowledge, all of the previous studies have been restricted to $m = 0$ multipoles. [20] have shown that including $\ell = 2$ and 4 with $m = 0$ in the analysis have only marginal effect on the cosmological parameter posteriors. A recent study by [30] has shown that the incorporation of $m \neq 0$ moments significantly improves the information gain. It is crucial to accurately measure the higher-order multipoles with $m \neq 0$ for precision cosmology.

Following the theoretical framework introduced by [25] and [26], in this paper, we present a fast and accurate estimator to calculate the bispectrum multipoles B_ℓ^m , including those with $m \neq 0$, considering triangles of all possible unique shapes.

A brief outline of the paper is as follows. Section II presents the Methodology where we describe the formalism and algorithm of the estimator. Section III presents the Validation of the estimator, including theoretical background, data simulation, and binning effects. Section IV presents the Summary and Discussion.

II. METHODOLOGY

The bispectrum $B^s(\mathbf{k}_1, \mathbf{k}_2, \mathbf{k}_3)$ of any random field in redshift space $\delta^s(\mathbf{x})$ distributed in a box of volume V is defined as,

$$B^s(\mathbf{k}_1, \mathbf{k}_2, \mathbf{k}_3) = V^{-1} \langle \Delta^s(\mathbf{k}_1) \Delta^s(\mathbf{k}_2) \Delta^s(\mathbf{k}_3) \rangle, \quad (1)$$

with $\mathbf{k}_1 + \mathbf{k}_2 + \mathbf{k}_3 = 0$ imposing that three \mathbf{k} vectors form a closed triangle. $\langle \dots \rangle$ denotes the average with respect to an ensemble of independent realizations, and $\Delta^s(\mathbf{k})$ is the Fourier transform of $\delta^s(\mathbf{x})$. The $\Delta^s(\mathbf{k})$ is statistically anisotropic along LoS, but isotropy is still preserved on the planes perpendicular to LoS. The bispectrum is invariant under the rotation of triangles about the LoS direction. Due to this symmetry and closed triangle con-

* sukhdeepsingh5ab@gmail.com

† somnathbharadwaj@gmail.com

¹ <https://www.sdss.org/>

² <https://www.desi.lbl.gov/>

³ <https://www.lsst.org/>

⁴ <https://www.euclid-ec.org/>

dition, the bispectrum is a function of 5 independent parameters. We opt for the parameterization prescribed by [25]. For a triangle with $\mathbf{k}_1 \geq \mathbf{k}_2 \geq \mathbf{k}_3$, its size is parameterized by $k_1 = |\mathbf{k}_1|$, shape by two dimensionless parameters

$$\mu = -\frac{\mathbf{k}_1 \cdot \mathbf{k}_2}{k_1 k_2}, \quad t = \frac{k_2}{k_1}, \quad (2)$$

and orientation with respect to the LoS direction \hat{z} by a unit vector $\hat{\mathbf{p}}$. The cosine of the angle between the three sides of the triangle and \hat{z} are respectively given by

$$\begin{aligned} \mu_1 &= p_z, & \mu_2 &= -\mu p_z + \sqrt{1 - \mu^2} p_x \\ \mu_3 &= \frac{-[(1 - t\mu)p_z + t\sqrt{1 - \mu^2} p_x]}{\sqrt{1 - 2t\mu + t^2}} \end{aligned} \quad (3)$$

Theoretically, we calculate the expansion coefficients of the bispectrum in terms of $Y_\ell^m(\hat{\mathbf{p}})$ the spherical harmonic basis using [25]

$$\bar{B}_\ell^m(k_1, \mu, t) = \sqrt{\frac{2\ell + 1}{4\pi}} \int [Y_\ell^m(\hat{\mathbf{p}})]^* B^s(\hat{\mathbf{p}}, k_1, \mu, t) d\Omega_{\hat{\mathbf{p}}}, \quad (4)$$

where the integration is over 4π steradian, corresponding to all possible orientations of a triangle of a fixed size (k_1) and shape (μ, t). From the observational point of view, we consider a finite volume V with N_g^3 grid points. The multipole moments can be calculated by identifying the set \mathcal{T} of all triangles of a fixed size (k_1) and shape (μ, t), and using

$$\bar{B}_\ell^m(k_1, \mu, t) = \sqrt{\frac{2\ell + 1}{4\pi}} \frac{\sum_{\mathcal{T}} [Y_\ell^m(\hat{\mathbf{p}})]^* B^s(\hat{\mathbf{p}}, k_1, \mu, t)}{\sum_{\mathcal{T}} |Y_\ell^m(\hat{\mathbf{p}})|^2}, \quad (5)$$

where $\sum_{\mathcal{T}}$ denotes a sum over all triangle orientations that are accessible in the 3D gridded data cube. The multipole moments $\bar{B}_\ell^m(k_1, \mu, t)$ (Eq.4) do not exactly match $\bar{B}_\ell^m(k_1, \mu, t)$ (Eq.5) because of the discrete sampling of \mathbf{k} space whereby the integration is replaced with a summation [20, 31]. We have accounted for this effect and will describe it in the next section.

The direct implication of Eq.5 is immensely time-consuming as it involves identifying triangles, which requires computations of order N_g^6 . Several earlier works by [13, 32, 33] have proposed an FFT based technique to compute binned statistics in Fourier space, which considerably speeds up the bispectrum computation. Following a similar formalism, [34] has proposed a fast estimator that considers spherical shells in \mathbf{k} space to compute the binned bispectrum monopole $\bar{B}_0^0(k_1, \mu, t)$. Further, this can be easily extended to estimate the higher multipoles with $m = 0$, as has been implemented in [35]. However, the $m \neq 0$ multipoles introduce additional complexity due to $e^{im\phi}$ phase factor in the spherical harmonics, which encapsulates the dependence on the azimuthal direction. It is not possible to incorporate this phase factor if we use spherical shells in \mathbf{k} space to compute the binned bispectrum. We have overcome this difficulty by considering

a different binning scheme, as shown in Fig.1. Here the box can be viewed as a collection of N_g 2D planes normal to \hat{z} . Each plane is uniformly divided into N_r concentric annular rings of width δk_\perp , and three such planes are shown in Fig.1. Decomposing a \mathbf{k} vector into components \mathbf{k}_\perp and k_\parallel that are respectively perpendicular and parallel to \hat{z} , the closed triangle condition yields to two conditions $k_{1\parallel} + k_{2\parallel} + k_{3\parallel} = 0$ and $\mathbf{k}_{1\perp} + \mathbf{k}_{2\perp} + \mathbf{k}_{3\perp} = 0$. The first condition constrains the choice of the three planes corresponding to $(k_{1\parallel}, k_{2\parallel}, k_{3\parallel})$. Here, we independently fix two planes namely $k_{1\parallel}$ and $k_{2\parallel}$, for which the third plane is determined using $k_{3\parallel} = -k_{1\parallel} - k_{2\parallel}$.

According to the second condition, the perpendicular components of the three wave vectors must form a closed triangle on the 2D plane perpendicular to \hat{z} . To estimate the binned bispectrum, we consider three annular rings labeled (a_1, a_2, a_3) respectively located in the planes $(k_{1\parallel}, k_{2\parallel}, k_{3\parallel})$. We define the binned bispectrum estimator as

$$\begin{aligned} \hat{B}^s(k_{1\perp}, k_{2\perp}, k_{3\perp}, k_{1\parallel}, k_{2\parallel}) &= \frac{1}{V N_{\text{tri}}} \sum_{\mathbf{k}_{1\perp}} \sum_{\mathbf{k}_{2\perp}} \sum_{\mathbf{k}_{3\perp}} \left[\Delta(\mathbf{k}_{1\perp}, k_{1\parallel}) \Delta(\mathbf{k}_{2\perp}, k_{2\parallel}) \right. \\ &\quad \left. \times \Delta(\mathbf{k}_{3\perp}, k_{3\parallel}) \right] \delta_{\mathbf{K}}(\mathbf{k}_{1\perp} + \mathbf{k}_{2\perp} + \mathbf{k}_{3\perp}), \end{aligned} \quad (6)$$

where $(\mathbf{k}_{1\perp}, \mathbf{k}_{2\perp}, \mathbf{k}_{3\perp})$ refer to the possible \mathbf{k}_\perp modes in (a_1, a_2, a_3) respectively. The 2D Kronecker delta function $\delta_{\mathbf{K}}(\mathbf{k}_{1\perp} + \mathbf{k}_{2\perp} + \mathbf{k}_{3\perp})$ ensures that the estimator picks up a contribution only when the three vectors $(\mathbf{k}_{1\perp}, \mathbf{k}_{2\perp}, \mathbf{k}_{3\perp})$ form a closed triangle, and N_{tri} is the total number of such triangles. Here, $(k_{1\perp}, k_{2\perp}, k_{3\perp})$ respectively refer to the mean wave number of the \mathbf{k}_\perp modes in (a_1, a_2, a_3) respectively.

The FFT implementation of Eq. 6 utilizes the Fourier expansion of the 2D Kronecker delta function

$$\delta_{\mathbf{K}}(\mathbf{k}_{1\perp} + \mathbf{k}_{2\perp} + \mathbf{k}_{3\perp}) = \frac{1}{N_g^2} \sum_{\mathbf{x}_\perp} \exp(-i[\mathbf{k}_{1\perp} + \mathbf{k}_{2\perp} + \mathbf{k}_{3\perp}] \cdot \mathbf{x}_\perp). \quad (7)$$

It is now possible to use this to express the estimator as

$$\begin{aligned} \hat{B}^s(k_{1\perp}, k_{2\perp}, k_{3\perp}, k_{1\parallel}, k_{2\parallel}) &= \frac{1}{V N_{\text{tri}}} \frac{1}{N_g^2} \sum_{\mathbf{x}_\perp} D(k_{1\perp}, k_{1\parallel}, \mathbf{x}_\perp) D(k_{2\perp}, k_{2\parallel}, \mathbf{x}_\perp) \\ &\quad \times D(k_{3\perp}, k_{3\parallel}, \mathbf{x}_\perp), \end{aligned} \quad (8)$$

where

$$D(k_{1\perp}, k_{1\parallel}, \mathbf{x}_\perp) = \sum_{\mathbf{k}_{1\perp}} \Delta(\mathbf{k}_{1\perp}, k_{1\parallel}) \exp(-i\mathbf{k}_{1\perp} \cdot \mathbf{x}_\perp), \quad (9)$$

which is the inverse FFT of the field $\Delta(\mathbf{k}_{1\perp}, k_{1\parallel})$ restricted to the annular ring a_1 . The other D s are similarly defined considering a_2 and a_3 .

We now calculate N_{tri} , the total number of triangles that appears in Eq. (8), using

$$N_{\text{tri}} = \sum_{\mathbf{k}_{1\perp}} \sum_{\mathbf{k}_{2\perp}} \sum_{\mathbf{k}_{3\perp}} \delta_{\mathbf{K}}(\mathbf{k}_{1\perp} + \mathbf{k}_{2\perp} + \mathbf{k}_{3\perp}). \quad (10)$$

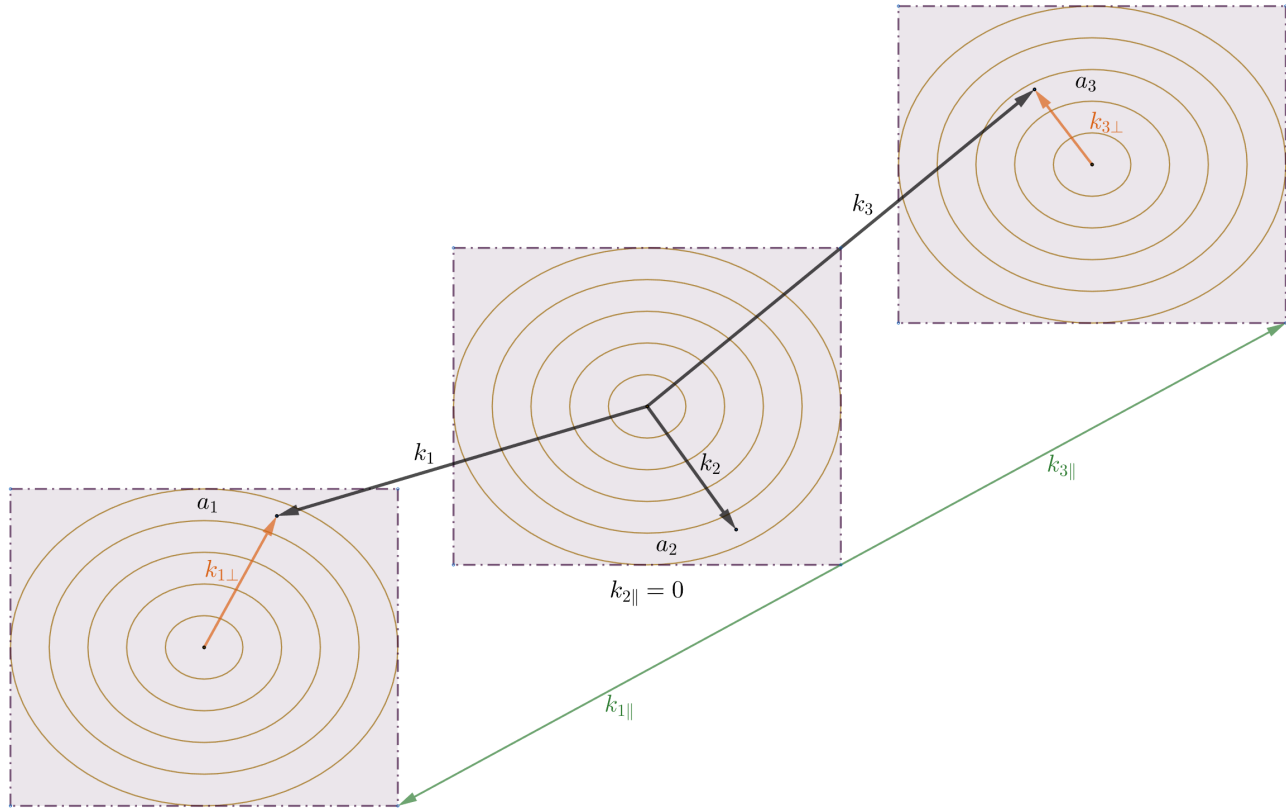


FIG. 1. The binning scheme of the estimator. This demonstrates the division of \mathbf{k} space into multiple planes perpendicular to the Line of Sight (LoS) direction \hat{z} , with each plane further subdivided into concentric annular rings. We show a closed triangle formed by three modes $\mathbf{k}_1, \mathbf{k}_2, \mathbf{k}_3$ that fall in different annular rings labeled as a_1, a_2, a_3 . The combination of three rings and planes defines a bin of triangles that have a fixed shape (μ, t), size (k_1), and orientation ($\hat{\mathbf{p}}$) with respect to LoS. If this triangle is rotated around the LoS such that three \mathbf{k} modes are restricted within respective annular rings, then the rotated triangle will still have the same orientation ($\hat{\mathbf{p}}$) relative to LoS as that of the original triangle. The bin contains all such triangles. The \mathbf{k} vectors are decomposed into their $k_{\parallel}\hat{z}$ and \mathbf{k}_{\perp} components with respect to LoS. Note that the middle plane is considered to be centered at the origin $\mathbf{k} = 0$ (hence $k_{2\parallel} = 0$) to avoid complexity in the illustration.

We have implemented Eq. (10) using

$$N_{\text{tri}} = \frac{1}{N_{\text{g}}^2} \sum_{\mathbf{x}_{\perp}} I(k_{1\perp}, \mathbf{x}_{\perp}) I(k_{2\perp}, \mathbf{x}_{\perp}) I(k_{3\perp}, \mathbf{x}_{\perp}), \quad (11)$$

where

$$I(k_{1\perp}, \mathbf{x}_{\perp}) = \sum_{\mathbf{k}_{1\perp}} \exp(-i\mathbf{k}_{1\perp} \cdot \mathbf{x}_{\perp}), \quad (12)$$

and the other I s are similarly defined using a_2 and a_3 .

The particular bin under consideration, for which we have calculated the binned bispectrum $\hat{B}^s(k_{1\perp}, k_{2\perp}, k_{3\perp}, k_{1\parallel}, k_{2\parallel})$, considers all closed triangles $(\mathbf{k}_1, \mathbf{k}_2, \mathbf{k}_3)$ that have $(k_{1\parallel}, k_{2\parallel}, k_{3\parallel})$ fixed, and $(\mathbf{k}_{1\perp}, \mathbf{k}_{2\perp}, \mathbf{k}_{3\perp})$ lie within the annular rings (a_1, a_2, a_3) respectively. Note that the binned bispectrum is a function of 5 independent parameters $(k_{1\perp}, k_{2\perp}, k_{3\perp}, k_{1\parallel}, k_{2\parallel})$, that describes the mean shape, size, and orientation with respect to \hat{z} . We use Eq. 2 and Eq. 3 to transform from $(k_{1\perp}, k_{2\perp}, k_{3\perp}, k_{1\parallel}, k_{2\parallel})$ to $(\hat{\mathbf{p}}, k_1, \mu, t)$, whereby we have the binned bispectrum estimator $\hat{B}^s(\hat{\mathbf{p}}, k_1, \mu, t)$ that

we use in Eq. 5 to calculate the multipole moments $\hat{B}_{\ell}^m(k_1, \mu, t)$. The resulting values of (k_1, μ, t) are not uniformly spaced, and we have further binned $\hat{B}_{\ell}^m(k_1, \mu, t)$ so as to uniformly sample the (k_1, μ, t) parameter space. The bin averaged values of $\hat{B}_{\ell}^m(k_1, \mu, t)$ are computed as the weighted mean using the number of triangles N_{tri} as weights.

III. VALIDATING THE ESTIMATOR

A. Theoretical expressions

To validate the estimator, we generate a mildly non-Gaussian random field in redshift space $\delta^s(\mathbf{x})$ for which the bispectrum multipole moments are analytically derived. We start with generating a Gaussian random field in real space $\delta_{\text{G}}^r(\mathbf{x})$ using a specified power spectrum $P(k)$ and introduce non-Gaussianity through a local quadratic

bias,

$$\delta^r(\mathbf{x}) = \delta_G^r(\mathbf{x}) + f_{\text{NG}} \{ [\delta_G^r(\mathbf{x})]^2 - \langle [\delta_G^r(\mathbf{x})]^2 \rangle \} \quad (13)$$

where the parameter f_{NG} controls the level of non-Gaussianity in the random field $\delta^r(\mathbf{x})$. The real space bispectrum B^r computed, to linear order in f_{NG} , is

$$B^r(k_1, k_2, k_3) = 2f_{\text{NG}} [P(k_1)P(k_2) + P(k_2)P(k_3) + P(k_3)P(k_1)]. \quad (14)$$

The field is mapped to redshift space by applying linear RSD,

$$\Delta^s(\mathbf{k}) = (1 + \beta_1 \mu_k^2) \Delta^r(\mathbf{k}). \quad (15)$$

where $\Delta^r(\mathbf{k})$ and $\Delta^s(\mathbf{k})$ are the Fourier transform of the field in real and redshift space respectively and β_1 is the linear RSD parameter. The linear RSD theory predicts the redshift space bispectrum $B^s(\hat{\mathbf{p}}, k_1, \mu, t)$ for this field to be,

$$B^s(\hat{\mathbf{p}}, k_1, \mu, t) = (1 + \beta_1 \mu_1^2)(1 + \beta_1 \mu_2^2)(1 + \beta_1 \mu_3^2) B^r(k_1, k_2, k_3). \quad (16)$$

The analytical expressions for the multipole moments $B_\ell^m(k_1, \mu, t)$ can be calculated using Eq.(4). These expressions are rather lengthy and hence not explicitly shown here. We refer the reader to Eqs. (24-29,31-33,A1-A7) of [25] for details. The analytical expressions are expected to hold true for sufficiently small values of f_{NG} such that $f_{\text{NG}} \sigma_G \ll 1$, where $\sigma_G^2 = \langle [\delta_G^r]^2 \rangle$ is the variance of $\delta_G^r(\mathbf{x})$.

B. Simulations

We simulated the field in a box of volume $V = L^3 = (215 \text{ Mpc})^3$ divided in $N_g = 384$ grids in each direction. The inter-grid spacing for the box comes out to be 0.56 Mpc and $k_{\text{min}} = 0.029 \text{ Mpc}^{-1}$. We use the input power spectrum $P(k) = k^{-2}$ to generate δ_G^r . The non-Gaussianity parameter is chosen to be $f_{\text{NG}} = 0.5$ for which $f_{\text{NG}} \sigma_G \approx 0.2$ and set linear RSD parameter $\beta_1 = 1$. We have generated 50 independent realizations of the field and used these to estimate the mean $\bar{B}_\ell^m(k_1, \mu, t) = \langle \tilde{B}_\ell^m(k_1, \mu, t) \rangle$ and also the 1σ error bars.

C. Binning and discreteness effects

In this work, we have validated the estimator by comparing the values of $\bar{B}_\ell^m(k_1, \mu, t)$ estimated from the simulations with the analytical predictions for the same quantities. However, the analytical predictions $[\bar{B}_\ell^m]_c$ presented in [25], which have been obtained by using Eq.(16) in Eq.(4), assume the continuum limit (as denoted by the subscript c). In reality, we only have discrete \mathbf{k} modes, and the integral in Eq.(4) is replaced by a sum in Eq.(5). We further bin the estimated $\bar{B}_\ell^m(k_1, \mu, t)$ in (k_1, μ, t) to increase the SNR and also obtained values at regular intervals of (k_1, μ, t) . For this, we introduce the discrete

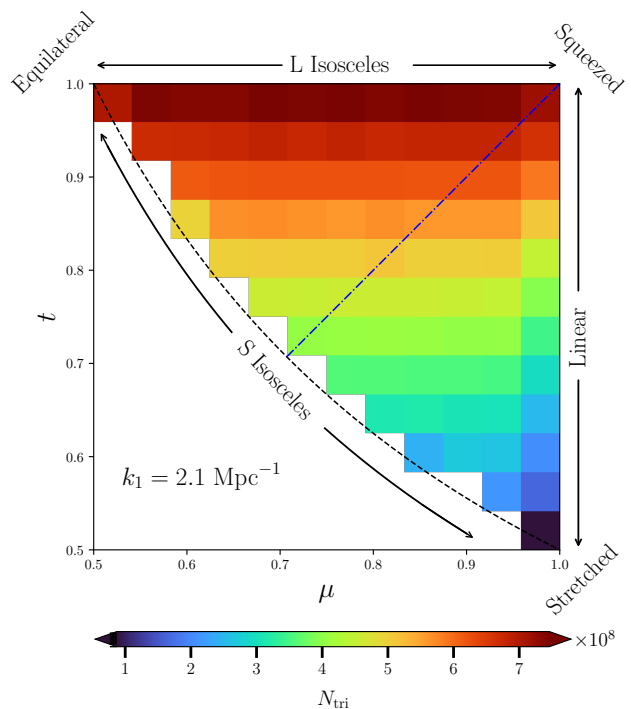


FIG. 2. Shows the total number of triangles N_{tri} of all possible shapes (μ, t) with a fixed size $k_1 = 2.1 \text{ Mpc}^{-1}$.

analytical predictions $[\bar{B}_\ell^m]_d$ (as denoted by the subscript d), which has been calculated by using the analytical predictions Eq.(16) in Eq.(5). The resulting predictions have also been binned in exactly the same way as for the estimator. In this work, we have validated the estimator by comparing $\bar{B}_\ell^m(k_1, \mu, t)$ with the analytical predictions $[\bar{B}_\ell^m]_d$.

Most theories which model the bispectrum, typically provide analytical predictions for $[\bar{B}_\ell^m]_c$. Therefore, it is often desirable to compare the estimated values $\bar{B}_\ell^m(k_1, \mu, t)$ with the analytical predictions $[\bar{B}_\ell^m]_c$ and not $[\bar{B}_\ell^m]_d$. A few earlier works [20, 31] have addressed this issue by introducing ‘discreteness weights’ $w_\ell^m(k_1, \mu, t)$

$$w_\ell^m(k_1, \mu, t) = \frac{[\bar{B}_\ell^m]_d(k_1, \mu, t)}{[\bar{B}_\ell^m]_c(k_1, \mu, t)} \quad (17)$$

which depend on the multipole moment (ℓ, m) , the triangle size and shape (k_1, μ, t) and possibly, also the theory under consideration. We have not considered this here, and we have directly compared \bar{B}_ℓ^m with $[\bar{B}_\ell^m]_d$.

D. Results

The $[\bar{B}_\ell^m]_c$ values are predicted to have a scale-invariant power-law k_1 dependence, and it is thus adequate to show the results for just a single value of k_1 . The number of triangles scales as $N_{\text{tri}} \propto k_1^6$ [36], and we have chosen a large value $k_1 = 2.1 \text{ Mpc}^{-1}$ with a bin

width $dk_1 = 0.2 \text{ Mpc}^{-1}$ so as to achieve a large value of N_{tri} and obtain a reliable (high signal to noise ratio: SNR) estimate of \bar{B}_ℓ^m . So as to accurately capture the shape dependence of $\bar{B}_\ell^m(k_1, \mu, t)$, we have divided the (μ, t) plane into fine bins of width $(d\mu, dt) = (0.04, 0.04)$ for evaluating the $\ell = 0$ and 2 multipoles. The values of \bar{B}_ℓ^m and the SNR are smaller for the higher multipoles $\ell > 2$, and we have used coarser (μ, t) bins for these.

Fig.2 illustrates the (μ, t) bins that we have used to parameterize the triangle shape dependence of $\bar{B}_\ell^m(k_1, \mu, t)$ for $\ell \leq 2$. It also shows N_{tri} the number of triangles corresponding to each bin. Considering the $\mu - t$ plane, the $\mu = 1$ boundary corresponds to linear triangles where the two larger sides of the triangle nearly aligned in the same direction. The $t = 1$ and $2\mu t = 1$ borders correspond to the L and S Isosceles triangles respectively. The two largest sides are equal for L Isosceles triangles, whereas the two smaller sides are equal for S. We see that in all cases the number of triangles is of the order of 10^8 , and it is largest for L Isosceles triangles. Further, N_{tri} decreases almost monotonically with decline in t , i.e., $N_{\text{tri}} \propto t$, and the number falls by a factor of 10 as triangles are deformed to the stretched limit. Nonetheless, N_{tri} does not vary significantly with μ .

Fig.3 shows the results for the $\ell = 0$ and 2 multipoles. Here, each row corresponds to a different combination of ℓ and m , as indicated in the figure. The panels in the left column show \bar{B}_ℓ^m estimated from the simulations. The analytical predictions $[\bar{B}_\ell^m]_d$ are visually indistinguishable from the \bar{B}_ℓ^m shown here, and we have not explicitly shown $[\bar{B}_\ell^m]_d$. The panels in the middle column show $\Delta_\ell^m = |\Delta \bar{B}_\ell^m| / \sigma \bar{B}_\ell^m$ where $\Delta \bar{B}_\ell^m = \bar{B}_\ell^m - [\bar{B}_\ell^m]_d$ is the difference between the estimated value and the analytical predictions, and $\sigma \bar{B}_\ell^m$ (estimated from the 50 realizations of the simulations) is the r.m.s. statistical fluctuations expected in $\Delta \bar{B}_\ell^m$. Δ_ℓ^m provides an estimate of whether the deviations between the estimator and analytical predictions are consistent with the expected statistical fluctuations or not. The panels in the right column show a comparison of \bar{B}_ℓ^m and $[\bar{B}_\ell^m]_d$ along the three boundaries of the $\mu - t$ plane.

We first consider the first row of Fig.3, which shows the results for $\ell = 0, m = 0$. We see that the value of the estimated \bar{B}_0^0 is minimum for equilateral triangles $((\mu, t) = (0.5, 1))$, and it increases as μ increases towards linear triangles $(\mu = 1)$. The top-most curve of the right panel shows the analytical prediction $[\bar{B}_0^0]_d(t)$ along the right boundary $(\mu \approx 1)$ of the $\mu - t$ plane. We see that \bar{B}_0^0 has the largest values along this curve. The value of $[\bar{B}_0^0]_d(t)$ further increases as we move from stretched triangles $((\mu, t) = (1, 0.5))$ to squeezed triangles $((\mu, t) = (1, 1))$ along this curve. The bottom-most curve shows $[\bar{B}_0^0]_d(\mu)$ along the top boundary $(t \approx 1)$ of the $\mu - t$ plane. Proceeding from equilateral to squeezed triangles along this curve, we see that $[\bar{B}_0^0]_d$ increases gradually till $\mu \approx 0.9$, beyond which it increases sharply close to the squeezed limit. The middle curve shows $[\bar{B}_0^0]_d(\mu)$ along the bottom boundary $(2\mu t \approx 1)$ of the $\mu - t$ plane. We see

that the value of $[\bar{B}_0^0]_d$ increases gradually as we proceed from equilateral to stretched triangles along this curve. In all cases, the estimated values \bar{B}_ℓ^m coincides with the analytical predictions $[\bar{B}_\ell^m]_d$, and the fractional deviations are within the range $[-0.033, 0.033]$. Considering the middle panel, we find that $\Delta_0^0 \leq 3$ across most of the $\mu - t$ plane, which indicates that the differences between the estimated values and the analytical predictions are largely within the expected statistical fluctuations. We have a few bins where $3 < \Delta_0^0 \leq 5$, which also may be consistent with the expected statistical fluctuations. In addition, there are a few bins where $5 < \Delta_0^0 \leq 7$ where the deviations are in excess of those expected from statistical fluctuations. The 4 bins where $5 < \Delta_0^0 \leq 7$ are all located near the squeezed limit, and a similar behaviour has been reported in earlier work [34]. The reason for this behaviour is that the bispectrum is very sensitive to the triangle shape near the squeezed limit, and the binned estimator includes triangles of different shapes due to the finite width of the annular rings (Fig. 1). In contrast, the analytical estimate only considers the bispectrum at the mean value of $(k_{1\perp}, k_{2\perp}, k_{3\perp}, k_{1\parallel}, k_{2\parallel})$ corresponding to the combination of three annular rings.

We next consider the quadrupole moment ($\ell = 2$) with $m = 0$, which is shown in the the second row of Fig.3. We see that the values of \bar{B}_2^0 are comparable to those of \bar{B}_0^0 . The results for \bar{B}_2^0 are also very similar to those for \bar{B}_0^0 , and the right and left panels of the second row are very similar to the corresponding panels of the first row. Considering the middle panel, we see that the deviations from the analytical predictions are within the expected statistical fluctuations ($\Delta_2^0 \leq 3$) for nearly all the bins, with the exception of two bins (both at $\mu \approx 1$) where $3 < \Delta_2^0 \leq 5$.

The third and fourth rows of Fig.3 show the quadrupole moment ($\ell = 2$) with $m = 1$ and $m = 2$ respectively. Unlike \bar{B}_0^0 and \bar{B}_2^0 , which are positive throughout, we see that \bar{B}_2^1 and \bar{B}_2^2 have both positive and negative values. The magnitude of \bar{B}_2^1 and \bar{B}_2^2 are ~ 4 times smaller than those of \bar{B}_0^0 and \bar{B}_2^0 . Further, the patterns in $\mu - t$ plane are also quite different. Considering \bar{B}_2^1 , we see that it has small positive values for acute triangles $(\mu < t)$, and negative values for obtuse triangles $(\mu > t)$, with values close to zero for right-angled triangles $(\mu = t)$. Considering the right panel, we see that that magnitude is largest for squeezed triangles where \bar{B}_2^1 is negative. We also note that the values of \bar{B}_2^1 are in good agreement with those of $[\bar{B}_2^1]_d$. The middle panel shows that $\Delta_2^1 \leq 3$ for all the bins except the squeezed triangles where $3 < \Delta_2^1 \leq 5$. Considering \bar{B}_2^2 , we see that the results are very similar to those for \bar{B}_2^1 . However, there is the difference that the values of \bar{B}_2^2 are positive over a large region of the $\mu - t$ plane as compared to \bar{B}_2^1 . We also see that $\Delta_2^2 \leq 3$ for nearly all the bins except a few (~ 6) where $3 < \Delta_2^2 \leq 5$.

Overall, we see that the estimated values \bar{B}_ℓ^m are in good agreement with the analytical predictions $[\bar{B}_\ell^m]_d$

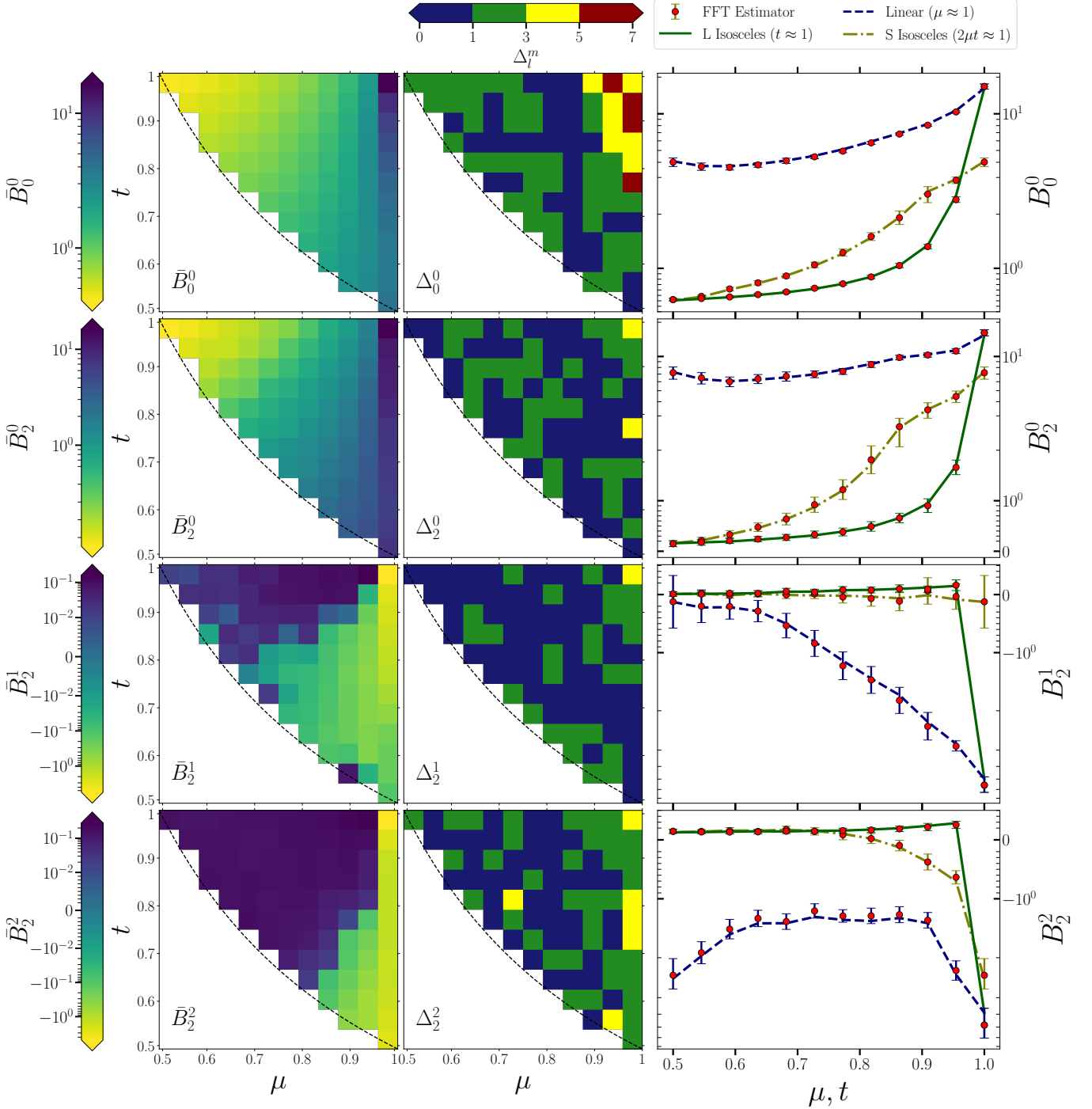


FIG. 3. Results for $\ell = 0$ and 2 multipoles. It shows the estimates and their deviation from analytical prediction for all triangle shapes (μ, t) having a fixed size $k_1 = 2.1 \text{ Mpc}^{-1}$. The uppermost row depicts the results for the monopole ($\ell = 0, m = 0$). The second, third, and fourth rows show $\ell = 2$ and $m = 0, 1, 2$ moments, respectively. The first column illustrates the mean estimates \bar{B}_ℓ^m from simulations. The second column shows $\Delta_\ell^m = |\Delta B_\ell^m| / \sigma B_\ell^m$, ΔB_ℓ^m is the deviation of the estimates from analytical predictions and σB_ℓ^m is the expected r.m.s. statistical fluctuation. The third column explicitly shows the estimated B_ℓ^m values (Red points with $5\sigma B_\ell^m$ error bars) for linear, L, and S Isosceles triangles. The various lines show the corresponding analytical predictions. Results are plotted against μ for L and S Isosceles triangles, and against t for linear triangles.

for the monopole moment ($\ell = 0, m = 0$), and all the quadrupole moments ($\ell = 2, m = 0, 1, 2$). We have carried out the same analysis for all the higher multipole moments, namely ($\ell = 4, m = 0, 1, 2, 3, 4$) and ($\ell = 6, m = 0, 1, 2, 3, 4, 5, 6$), that are predicted to be non-zero for our model [25]. The results for $\ell = 4$ and 6 are respectively presented in Figures 4 and 5 of Appendix A. In all the cases, we find that the values of \bar{B}_ℓ^m are in good agreement with the analytical predictions $[\bar{B}_\ell^m]_d$. The values of Δ_ℓ^m are mostly in the range $\Delta_\ell^m \leq 3$, and they are in the range $3 < \Delta_\ell^m \leq 5$ for a few bins, indicating that the deviations between \bar{B}_ℓ^m and $[\bar{B}_\ell^m]_d$ are consistent with that expected from statistical fluctuations.

IV. SUMMARY AND DISCUSSION

The bispectrum is the lowest-order statistic sensitive to non-Gaussianity in the underlying density field. This is particularly relevant for the late-time matter distribution where non-Gaussianity develops due to non-linear evolution [37], and the bispectrum contains a wealth of cosmological information [10, 19–21, 30, 38]. The redshifted 21-cm signal from the Epoch of Reionization is also predicted to be highly non-Gaussian due to the emergence of large ionized regions [39], and the bispectrum [35, 40–42] is expected to carry a plethora of information regarding the nature of the ionizing sources. It is therefore crucial to go beyond the power spectrum, and consider the bispectrum, and other higher-order statistics, to extract the maximum information from observational data.

The bispectrum is a function of the closed triangles formed by three \mathbf{k} vectors. Cosmological density fields are expected to be isotropic, and the bispectrum is predicted to depend only on the size and shape of the triangle, which we have parameterized using three parameters k_1 and (μ, t) respectively. However, due to redshift space distortion, the observed bispectrum also depends on how the triangle is oriented with respect to the LoS, and we require five parameters to parameterize the redshift space bispectrum. Here we have considered the redshift space bispectrum $B^s(\hat{\mathbf{p}}, k_1, \mu, t)$, where the unit vector $\hat{\mathbf{p}}$ [25] quantifies the orientation of the triangle with respect to the LoS. We have decomposed $B^s(\hat{\mathbf{p}}, k_1, \mu, t)$ into the spherical harmonic basis $Y_\ell^m(\hat{\mathbf{p}})$ (eq. 4), and use the bispectrum multipole moments $\bar{B}_\ell^m(k_1, \mu, t)$ to quantify the RSD anisotropy.

It is relatively straightforward to compute the bispectrum by looping over the available \mathbf{k} vectors, however, this is computationally very expensive as the computing time scales as $\sim N_g^6$ for a 3D data cube of N_g grids in each dimension. This limitation is overcome by several FFT-based fast bispectrum estimators where the computational time scales as $\sim N_g^3 \log(N_g)$ [13, 32, 33]. However, these estimators consider spherical shells in \mathbf{k} space, and they are restricted to the $m = 0$ multipoles [20, 43] of the redshift space bispectrum. Considering the multipole moments with $\ell \leq 6$, we only have four non-zero

multipole moments if we are restricted to $m = 0$, whereas we have a total of sixteen non-zero multipole moments if we also include the ones with $m \neq 0$ [26]. The difficulty arises due to the $e^{im\phi}$ term in $Y_\ell^m(\hat{\mathbf{p}})$, as it is not possible to evaluate this with spherical shells in \mathbf{k} space. We have overcome this by dividing the \mathbf{k} space into N_g planes perpendicular to the LoS, and dividing each plane into N_r annular rings. The combination of three rings and three planes contains all the triangles of a fixed size, shape, and orientation to the LoS. We have used FFT to evaluate the bispectrum for such a combination, and we average this over different orientations to evaluate the bispectrum multipole moments (eq. 5). The computational time to estimate the bispectrum for each combination of planes scales as $\sim N_g^2 \log(N_g)$, and we have $\sim N_g^3 \log(N_g)$ considering all N_g planes.

We have validated our estimator using simulations. We have considered 50 realizations of a mildly non-Gaussian field that incorporates redshift space distortion. The analytical expressions for bispectrum multipoles of this field are presented in [25]. We have used the estimator to calculate all the bispectrum multipoles that are predicted to be non-zero (up to $\ell = 6, m = 6$ in our case). We find that the estimated values \bar{B}_ℓ^m are in good agreement with the analytical predictions $[\bar{B}_\ell^m]_d$ for all the cases. The deviations of the estimates from the analytical predictions are within $\pm 3\sigma$ for most of the bins, consistent with their arising from statistical fluctuations. In a few bins, the deviations are in the range $\pm 3\sigma$ to $\pm 5\sigma$, which also is possibly due to statistical fluctuations. In some rare cases, mostly near the squeezed limit, we have deviations in the range $\pm 5\sigma$ to $\pm 7\sigma$. However, in these cases, the fractions deviations are of the order of 1% or smaller. In conclusion, our estimator is able to calculate all the non-zero bispectrum multipole moments at a high level of accuracy. It is anticipated that including the $m \neq 0$ multipoles will add to the information already available from galaxy redshift surveys, and that expected from future redshifted 21-cm observations.

ACKNOWLEDGEMENTS

SSG acknowledges the support of the Prime Minister Research Fellowship (PMRF). We thank Abinash Kumar Shaw for the useful discussions. We acknowledge the National Supercomputing Mission (NSM) for providing computing resources of ‘PARAM Shakti’ at IIT Kharagpur, which is implemented by C-DAC and supported by the Ministry of Electronics and Information Technology (MeitY) and Department of Science and Technology (DST), Government of India.

DATA AVAILABILITY

The simulated data and package involved in this work will be shared on reasonable request to the authors.

- [1] D. G. York et al. (SDSS), *Astron. J.* **120**, 1579 (2000), arXiv:astro-ph/0006396.
- [2] M. Levi et al. (DESI), arXiv e-prints , arXiv:1308.0847 (2013), arXiv:1308.0847 [astro-ph.CO].
- [3] v. Ivezić et al. (LSST), *Astrophys. J.* **873**, 111 (2019), arXiv:0805.2366 [astro-ph].
- [4] R. Laureijs et al. (EUCLID), arXiv e-prints , arXiv:1110.3193 (2011), arXiv:1110.3193 [astro-ph.CO].
- [5] E. Sefusatti, M. Liguori, A. P. S. Yadav, M. G. Jackson, and E. Pajer, *JCAP* **12**, 022, arXiv:0906.0232 [astro-ph.CO].
- [6] J. R. Fergusson, M. Liguori, and E. P. S. Shellard, *JCAP* **12**, 032, arXiv:1006.1642 [astro-ph.CO].
- [7] F. Oppizzi, M. Liguori, A. Renzi, F. Arroja, and N. Bartolo, *JCAP* **05**, 045, arXiv:1711.08286 [astro-ph.CO].
- [8] Y. Akrami et al. (Planck), *Astron. Astrophys.* **641**, A9 (2020), arXiv:1905.05697 [astro-ph.CO].
- [9] M. Shiraiishi, *Front. Astron. Space Sci.* **6**, 49 (2019), arXiv:1905.12485 [astro-ph.CO].
- [10] H. A. Feldman, J. A. Frieman, J. N. Fry, and R. Scoccimarro, *Phys. Rev. Lett.* **86**, 1434 (2001), arXiv:astro-ph/0010205.
- [11] R. Scoccimarro, *Phys. Rev. D* **70**, 083007 (2004), arXiv:astro-ph/0407214.
- [12] M. Liguori, E. Sefusatti, J. R. Fergusson, and E. P. S. Shellard, *Adv. Astron.* **2010**, 980523 (2010), arXiv:1001.4707 [astro-ph.CO].
- [13] R. Scoccimarro, *Phys. Rev. D* **92**, 083532 (2015), arXiv:1506.02729 [astro-ph.CO].
- [14] M. Ballardini, W. L. Matthewson, and R. Maartens, *Mon. Not. Roy. Astron. Soc.* **489**, 1950 (2019), arXiv:1906.04730 [astro-ph.CO].
- [15] D. W. Pearson and L. Samushia, *Mon. Not. Roy. Astron. Soc.* **478**, 4500 (2018), arXiv:1712.04970 [astro-ph.CO].
- [16] D. Babich, P. Creminelli, and M. Zaldarriaga, *JCAP* **2004**, 009 (2004), arXiv:astro-ph/0405356 [astro-ph].
- [17] N. Bartolo, E. Komatsu, S. Matarrese, and A. Riotto, *Phys. Rept.* **402**, 103 (2004), arXiv:astro-ph/0406398.
- [18] W. Sohn, A. Lazanu, P. Brax, and J. R. Fergusson, arXiv e-prints , arXiv:2311.13819 (2023), arXiv:2311.13819 [astro-ph.CO].
- [19] R. Scoccimarro, H. M. P. Couchman, and J. A. Frieman, *Astrophys. J.* **517**, 531 (1999), arXiv:astro-ph/9808305.
- [20] M. M. Ivanov, O. H. E. Philcox, G. Cabass, T. Nishimichi, M. Simonović, and M. Zaldarriaga, *Phys. Rev. D* **107**, 083515 (2023), arXiv:2302.04414 [astro-ph.CO].
- [21] O. H. E. Philcox, M. M. Ivanov, G. Cabass, M. Simonović, M. Zaldarriaga, and T. Nishimichi, *Phys. Rev. D* **106**, 043530 (2022), arXiv:2206.02800 [astro-ph.CO].
- [22] G. D’Amico, Y. Donath, M. Lewandowski, L. Senatore, and P. Zhang, arXiv e-prints , arXiv:2206.08327 (2022), arXiv:2206.08327 [astro-ph.CO].
- [23] S. Matarrese, L. Verde, and A. F. Heavens, *Mon. Not. Roy. Astron. Soc.* **290**, 651 (1997), arXiv:astro-ph/9706059.
- [24] R. Scoccimarro, H. M. P. Couchman, and J. A. Frieman, *Astrophys. J.* **517**, 531 (1999), arXiv:astro-ph/9808305 [astro-ph].
- [25] S. Bharadwaj, A. Mazumdar, and D. Sarkar, *mnras* **493**, 594 (2020), arXiv:2001.10243 [astro-ph.CO].
- [26] A. Mazumdar, S. Bharadwaj, and D. Sarkar, *mnras* **498**, 3975 (2020), arXiv:2005.07066 [astro-ph.CO].
- [27] J. Byun and E. Krause, *mnras* **10.1093/mnras/stac2313** (2022), arXiv:2205.04579 [astro-ph.CO].
- [28] P. Gagrani and L. Samushia, *mnras* **467**, 928 (2017), arXiv:1610.03488 [astro-ph.CO].
- [29] M. Tellarini, A. J. Ross, G. Tasinato, and D. Wands, *JCAP* **2016**, 014 (2016), arXiv:1603.06814 [astro-ph.CO].
- [30] C. Heinrich, O. Dore, and E. Krause, arXiv e-prints , arXiv:2311.13082 (2023), arXiv:2311.13082 [astro-ph.CO].
- [31] M. M. Ivanov, O. H. E. Philcox, T. Nishimichi, M. Simonović, M. Takada, and M. Zaldarriaga, *Phys. Rev. D* **105**, 063512 (2022), arXiv:2110.10161 [astro-ph.CO].
- [32] E. Sefusatti, Ph.D. thesis, Probing fundamental physics with large-scale structure: From galaxy formation to inflation, Polytechnic University, United States (2005).
- [33] D. Jeong, Ph.D. thesis, Cosmology with high ($z > 1$) redshift galaxy surveys, Univ. Texas at Austin (2010).
- [34] A. K. Shaw, S. Bharadwaj, D. Sarkar, A. Mazumdar, S. Singh, and S. Majumdar, *JCAP* **2021**, 024 (2021), arXiv:2107.14564 [astro-ph.CO].
- [35] S. S. Gill, S. Pramanick, S. Bharadwaj, A. K. Shaw, and S. Majumdar, *mnras* **527**, 1135 (2024), arXiv:2310.15579 [astro-ph.CO].
- [36] A. Mazumdar, D. Sarkar, and S. Bharadwaj, *mnras* **520**, 2534 (2023), arXiv:2209.03233 [astro-ph.CO].
- [37] P. J. E. Peebles, *The large-scale structure of the universe* (Princeton University Press, 1980).
- [38] H. Gil-Marín, J. Noreña, L. Verde, W. J. Percival, C. Wagner, M. Manera, and D. P. Schneider, *Mon. Not. Roy. Astron. Soc.* **451**, 539 (2015), arXiv:1407.5668 [astro-ph.CO].
- [39] S. Bharadwaj and S. K. Pandey, *mnras* **358**, 968 (2005), arXiv:astro-ph/0410581 [astro-ph].
- [40] S. Majumdar, J. R. Pritchard, R. Mondal, C. A. Watkinson, S. Bharadwaj, and G. Mellema, *MNRAS* **476**, 4007 (2018), arXiv:1708.08458 [astro-ph.CO].
- [41] A. Hutter, C. A. Watkinson, J. Seiler, P. Dayal, M. Sinha, and D. J. Croton, *MNRAS* **492**, 653 (2020), arXiv:1907.04342 [astro-ph.CO].
- [42] C. A. Watkinson, C. M. Trott, and I. Hothi, *mnras* **501**, 367 (2021), arXiv:2002.05992 [astro-ph.CO].
- [43] F. Rizzo, C. Moretti, K. Pardede, A. Eggemeier, A. Odfo, E. Sefusatti, C. Porciani, and P. Monaco, *JCAP* **2023**, 031 (2023), arXiv:2204.13628 [astro-ph.CO].

Appendix A: Results for $\ell = 4$ and 6

Fig.4 and 5 shows the results for $\ell = 4$ and 6 bispectrum multipoles respectively. The estimates for all the cases are in good statistical agreement with the analytical predictions. The statistical deviation is $\Delta_{\ell}^m \leq 3$ for most of the cases, and it is in the range $3 < \Delta_{\ell}^m \leq 5$ for a few bins near linear triangles.

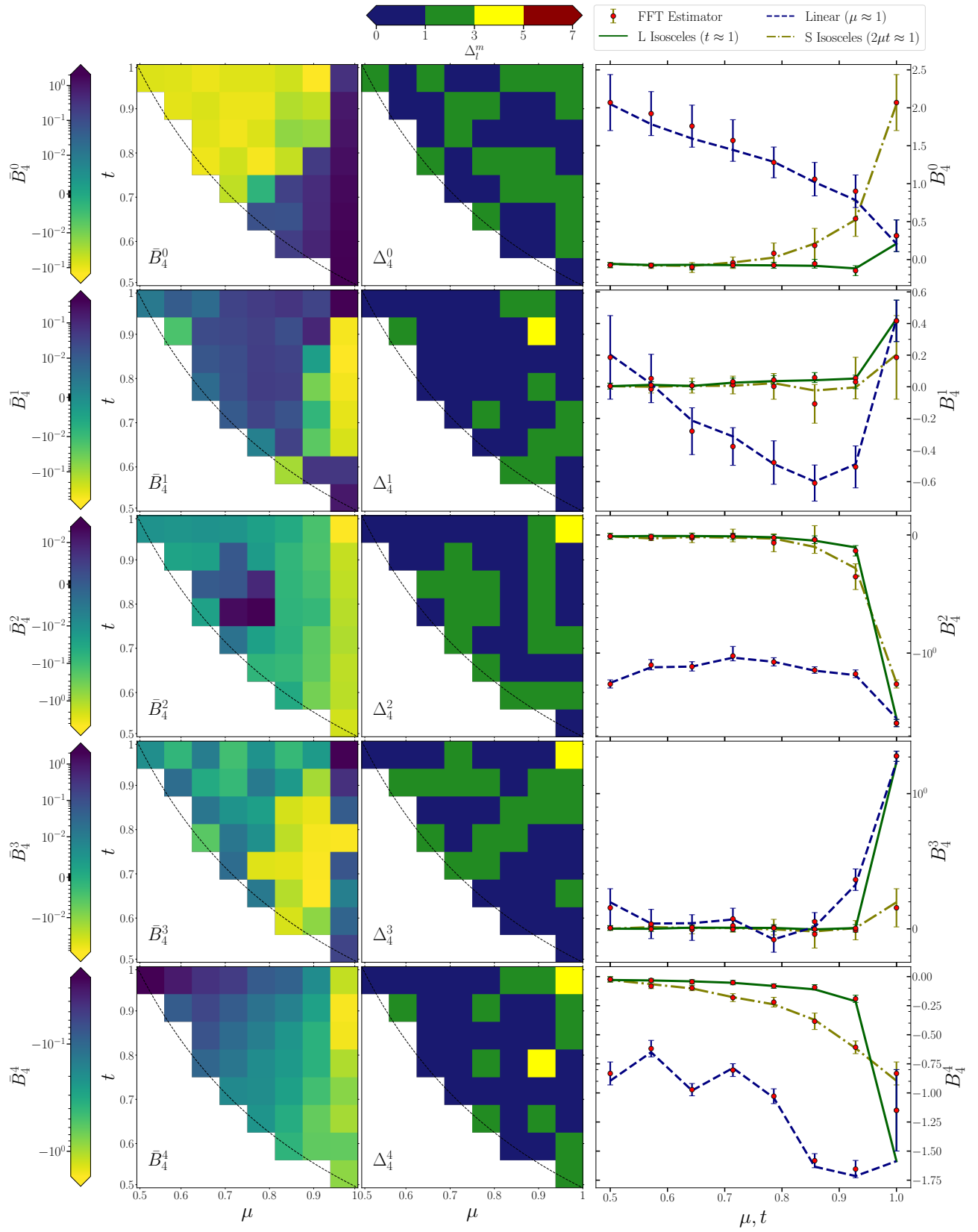


FIG. 4. Results for $\ell = 4$ multipoles (panels are same as in Fig.3). The error bars in the right panel are $3\sigma_{B_\ell^m}$ r.m.s fluctuations.

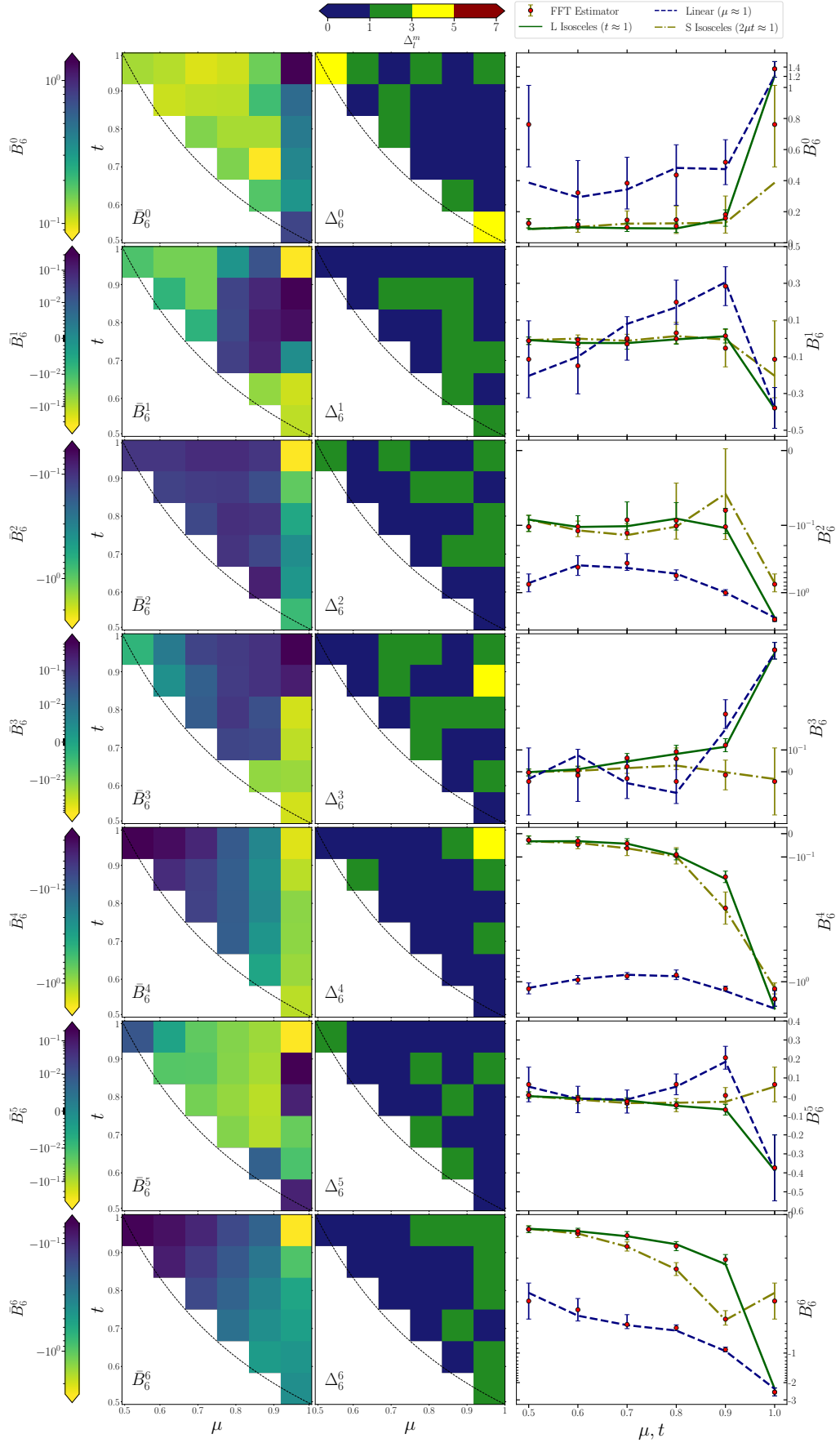


FIG. 5. Results for $\ell = 6$ multipoles (panels are same as in Fig.3). The error bars in the right panel are $3\sigma_{B_\ell^m}$ r.m.s fluctuations.